Over-the-Air Characterization Techniques for Antenna-Coupled Direct-Detectors at Terahertz Frequencies

Hoogelander, M.; Alonso Del Pino, M.; Llombart, N.; Spirito, M.

DOI
10.1109/IMS37964.2023.10187910

Publication date
2023

Document Version
Final published version

Published in
Proceedings of the 2023 IEEE/MTT-S International Microwave Symposium, IMS 2023

Over-the-Air Characterization Techniques for Antenna-Coupled Direct-Detectors at Terahertz Frequencies

M. Hoogelander, M. Alonso-delPino, N. Llombart, M. Spirito
Delft University of Technology, Microelectronics Department, The Netherlands
m.hoogelander@tudelft.nl

2023 IEEE/MTT-S International Microwave Symposium - IMS 2023 | 979-8-3503-4764-7/23/$31.00 ©2023 IEEE | DOI: 10.1109/IMS37964.2023.10187910

***Abstract*—The continuous advancements in the coverage and sensitivity of terahertz direct-detector imagers places increasing constraints on the test benches needed for characterization. Already, relative differences on the order of a few decibels are observed between simulated and measured performance in the state-of-the-art literature. This contribution elaborates on our experimental strategies to maximize the characterization accuracy and precision of terahertz direct-detection imagers using a broadband, over-the-air measurement procedure. As a demonstration, four elements within a dense detector array were characterized in the WR2.2 band. By optimizing the modulation frequency in the setup for minimal impact of low-frequency noise and interference, a measurement dynamic range up to 30 dB was achieved, including the path loss over 20 cm. The hardware-to-model agreement of the characterized array is below 1 dB between 325 and 450 GHz.**

***Keywords* —Terahertz imaging, direct-detection, over-the-air measurement, antenna measurement, modulation, wideband measurement, antenna array.**

I. Introduction

The performance of antenna-coupled direct-detectors operating in the terahertz regime has shown substantial progress over the past decade, both in terms of scalability and sensitivity. A detector array comprising a large number of elements was reported in [1], while in [2] an array design featuring a high density of the elements was presented. Moreover, the demonstrated noise equivalent power (NEP) of THz direct-detectors is gradually approaching unity $\mathrm{pW}/\sqrt{\mathrm{Hz}}$ [3]-[6]. Combined, these advancements indicate that the objective of realizing un-cooled, near real-time passive imaging systems [5] at sub-mm wavelengths integrated in a silicon-based technology could be reached in the near future.

Various works presented comprehensive modelling steps to obtain an accurate prediction of the detector performance at the system level [5], [6]. Less attention, however, has been given in literature to elaborate on the various challenges involved in acquiring equally accurate measurements. Because the detectors and antennas are co-integrated, the characterization is often performed over-the-air using an active, coherent source for illumination. Modulation of this source is necessary [1]-[6] to overcome the low-frequency noise injected by the device-under-test (DUT) and thus to achieve an adequate measurement dynamic range (DR). Often, an amplification stage is needed before signal acquisition [3]-[6], the bandwidth of which places a limit on the modulation frequency. These relatively complex test benches require careful assembly, alignment and multiple calibration steps in both the transmission and readout chains before precise and accurate measurements can be obtained.

Recent literature shows that it remains challenging to acquire characterization results that match the simulated performance within 1 dB [4], [6], [7]. Mostly, the discrepancies between the modelled and realized behavior are attributed to process variations and (finite) array effects, but little consideration is being given to any impact of the errors introduced by the measurement procedure itself.

In this contribution, we present a detailed experimental analysis of the implementation of the transmission chain and an optimization of the modulation frequency to maximize the measurement accuracy and precision. The DUT is a dense connected array design with integrated square-law detectors consisting of Schottky Barrier Diodes (SBD), and operates from 200 to 600 GHz [2]. The array is implemented in the 22 nm CMOS node and the die is fixed to a silicon, elliptical lens with a diameter of 7.6 cm, which is coated with a parylene-C layer to reduce reflection losses.

The paper is organized as follows: first, the analysis and optimization of the characterization setup is discussed. In Section III the measurement results of the DUT are presented in terms of radiation patterns and system responsivity, and a conclusion is given in Section IV.

II. Analysis of the Experimental Setup

A simplified schematic of the broadband, over-the-air characterization setup is shown in Fig. 1. On the transmit side of the setup is a coherent source for illumination of the DUT, consisting of a WR2.2 extender module from VDI equipped with a standard 20 dB rectangular horn. The input to the extender module is modulated to overcome the DR deterioration at the readout side due to the low-frequency noise of the detector. An IQ mixer from MITEQ implements the modulation step by chopping the CW signal, which in turn is

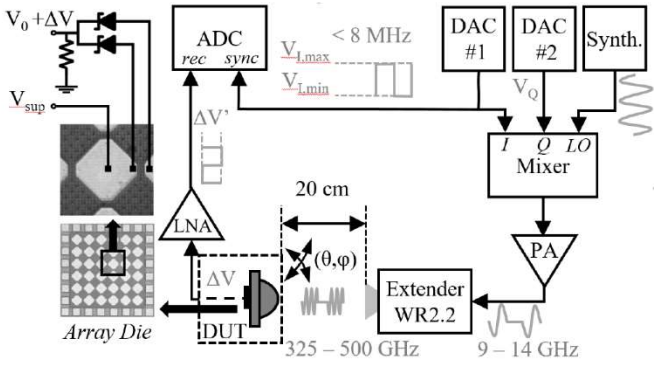

Fig. 1. Schematic of characterization setup and micrograph of CMOS array.

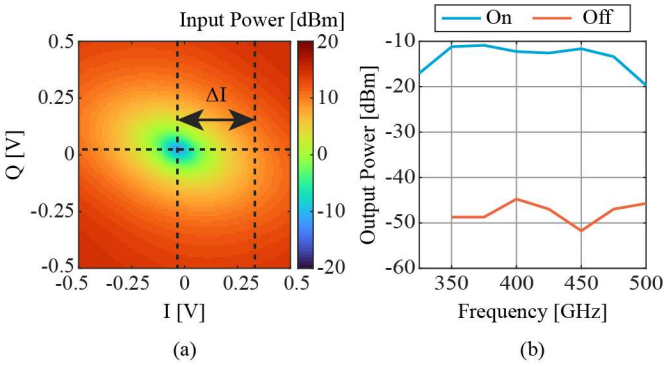

Fig. 2. I and Q voltage sweeps per frequency at the extender input to identify the optimal mixer drive levels, example for a 400 GHz output (a). Achievable on/off power levels from the extender output versus frequency (b).

generated using an Anritsu MG3694A synthesizer. The magnitude and frequency of the modulation was made user-defined by using a set of DACs to drive the IQ ports of the mixer. On the receive side of the setup, the DUT is mounted on a two-axis rotational stage (e.g. gimbal) with 0.02 degree accuracy. By rotating the DUT, the beams of the individual elements within the array can be conveniently aligned to the horn antenna. The source and the DUT are spaced 20 cm apart, to ensure that the horn is in the far-field of the silicon lens of the DUT and vice versa. The flexibility provided by this gimbal is crucial, given the mechanical tolerances in the assembly of the DUT and the setup. The output voltage of the DUT is amplified by a Texas Instruments INA-849 LNA before being digitized by a 100MS/s, 14-bit ADC card from NI.

A. Modulation of the THz source

On-off switching, or "chopping", of the THz signal is an effective modulation scheme to mitigate the effect of low-frequency noise injected at the receiver side of the setup. As depicted in Fig. 1, this can be realized by presenting an equivalently modulated signal to the input of the frequency extender. To maximize the measurement DR, the extenders need to be driven to saturation during the on-state, and receive minimal input power during the off-state. In this work, the driving levels according to these conditions were determined by evaluating the power at the PA output versus the I and Q voltages of the mixer for all operating frequencies of interest. The driving voltages corresponding to extender saturation and minimal LO leakage were found from the resulting voltages versus power surfaces, such as the one shown in Fig. 2(a).

In order to extract the responsivity of the DUT from its output response, the available power from the active source needs to be known accurately. The power available at the output of the extender module was measured (in continuous operation) using a PM5 power meter and is shown in Fig. 2(b) for the on-, and off-states. Since the THz signal is modulated, it is tempting to use the power measured during modulation to extract the responsivity. However, the spurious content generated by the strongly non-linear extender module when a fast amplitude modulation is applied at its input will be averaged by the slow PM5 detector. When using the average power during modulated operation to compute the (peak) power during the on-state, the additional harmonic content results in an overestimation up to 0.7 dB for a 1 MHz modulation frequency. For this reason, only the power measured during CW operation is used to extract the responsivity. It should be noted that this is method is only valid if the detector/readout is fast enough to capture the envelope of the modulated signal and does not detect this spurious content.

B. Evaluation of Measurement Accuracy and Precision

The readout of the DUT consists of an LNA and a subsequent ADC, see Fig. 1. A second input channel of the ADC card is used to capture the square wave generated by the DAC. Using this information, different recordings of the ADC are synchronized, which can realize an integration time longer than the memory of the ADC card allows for (i.e. 84 ms). The variable gain of the LNA was set to 40 dB, yielding a bandwidth of 8 MHz and an input-referred noise floor of 1.5 $\mathrm{nV}/\sqrt{\mathrm{Hz}}$. This gain setting allows acquisition of a down-converted signal up to the MHz-range, where the 1/f noise corner of the DUT is expected to be located [5].

The voltage response $\Delta V'$, which is the peak-to-peak swing of the detected envelope at the LNA output, can be reconstructed from the frequency spectrum. Using the magnitude of the fundamental tone, $\Delta V'$ can be determined by recalling that the peak-to-peak swing of a square wave is a factor π larger than this tone in the (double-sided) spectrum. This approach also avoids integration of the spurious content generated by the extender module in the detected signal.

The expected response of a detector with a given voltage responsivity $\Re_{v,sys}$, can be found by using the Friis equation:

$$\Delta V' = \frac{P_{src,CW} G_{horn} A_{lens} \Re_{v,sys} G_{LNA}}{4\pi d^2}, \quad (1)$$

where $P_{src,CW}$ is the power radiated from the horn with gain G_{hor} during the on-state, A_{lens}, the frontal area of the lens, G_{LNA} the LNA gain, and d the separation between the lens and the horn. If the DUT is to be characterized down to responsivity levels of 1 V/W, it can be deducted from (1) that a $\Delta V'$ on the order of tens of microvolts is expected. This magnitude is small, considering that the minimum selectable quantization step size of the ADC is 12 µV, and underlines that having a high sampling rate available is crucial. Using a sufficient oversampling rate, the quantization limit of the ADC can be improved beyond its physical number of bits and can therefore make up for the limited use of the digitization range [8].

To validate our procedure, the power at the fundamental tone and the average noise in its surrounding 20% bandwidth were measured as a function of modulation frequency for different bias voltages, the result of which is shown in Fig. 3(a). There are three interesting regions that can be distinguished in this figure. First, a band can be observed in which the modulation tone is always detected (Low DR), even when little or no bias voltage is applied. This peak remained visible when the DUT was removed from the loop (by shorting the LNA input) and is therefore the result of a low-level coupling within the setup. Since this contribution is deterministic, it could be removed in post-processing. A better approach, however, is to avoid unnecessary post-processing steps by selecting a

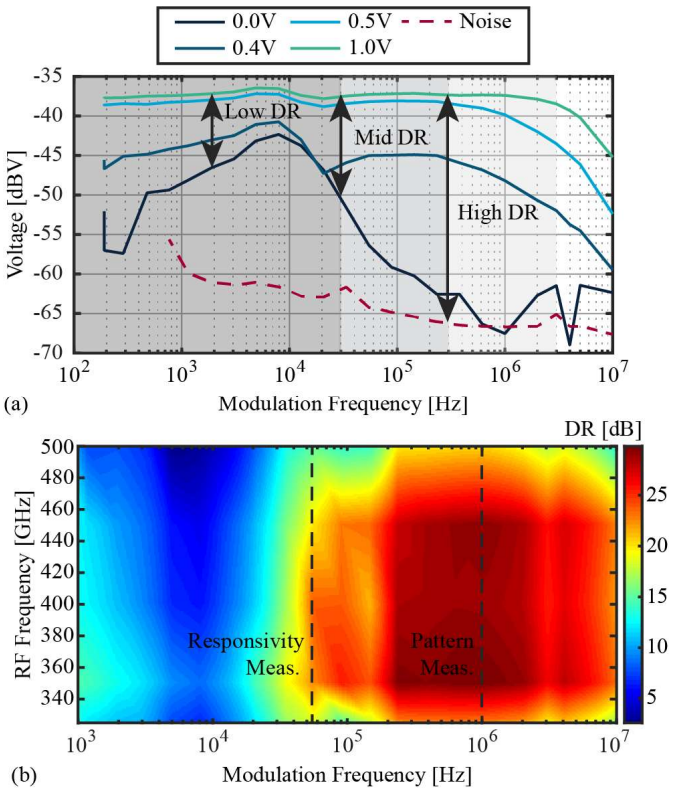

Fig. 3. Output voltage spectrum at the fundamental tone and average noise in a 20 % bandwidth versus modulation frequency for different bias voltages (a), and the DR at 1.0 V bias (b). An integration time of 100 x 10.2 ms was used.

modulation frequency beyond this band (e.g. > 20 kHz). Secondly, the magnitude of the fundamental tone remains constant within 0.5 dB up to 1 MHz, indicating that the detector is capable of following the square-wave envelope, and thus that the approach to estimate the response is valid. Lastly, it can be observed that the cut-off (modulation) frequency drops with the bias voltage. This behaviour affects the measurement precision at low bias voltages and is likely the result of the increasing impact of interconnect and loading capacitances due to a smaller diode junction capacitance. This effect places an upper bound on the modulation frequency when characterizing the system at low bias levels. When the dependence on bias voltage is not of interest, i.e. when measuring radiation patterns, a higher modulation frequency can be selected. As can be seen in Fig. 3(b), a DR up to 30 dB (including path loss) is achieved between 350 GHz and 450 GHz.

III. Characterization of a CMOS-Integrated Direct-Detector Array

The techniques discussed in the previous sections were used to characterize the radiation patterns and responsivity of the DUT with optimum DR. This section presents the results and discusses the discrepancies compared to the simulated behavior.

C. Radiation Patterns

The radiation patterns of several elements were measured over a scanning range of $\pm 20^{o}$, centered around their individual maxima along four cuts over the frequency band of interest. The bias voltage was fixed to 1 V and consequently a high modulation frequency of 1 MHz was selected to provide maximum DR, as was indicated in Fig. 3(b). The captured signal was integrated over a total time of 1.05 s.

The resulting radiation patterns of one of the elements near the array center are shown in Fig. 4(a)-(c). A very good agreement with simulations is obtained for the main lobe across the band. The DR degrades at 325 GHz and 500 GHz due to a drop of available power from the extender module (see Fig. 2(b)). Despite the high DR of the measurement setup, truncation of the patterns was necessary to prevent including the noise floor when computing the directivity. The integration range is smaller at the extremes of WR2.2 band, as indicated in Fig. 4(a) and (c). To obtain a better benchmark for the measured directivity, the same cuts and truncation were also applied to the simulated 2D patterns.

As can be seen in Fig. 4(d), the measured directivity of four centrally located elements lies within 1 dB of the value expected from simulations up to 450 GHz. At higher frequencies, any mechanical tolerances in the fabrication and assembly have a higher impact, which could explain the increasing mismatch. An opposite, but smaller, mismatch can be observed around 325 GHz, where the relatively high directivity could be explained by the effect of higher mutual coupling between the array elements [9]. The inset of Fig. 4(d) shows additional frequency points in the 396 – 404 GHz band

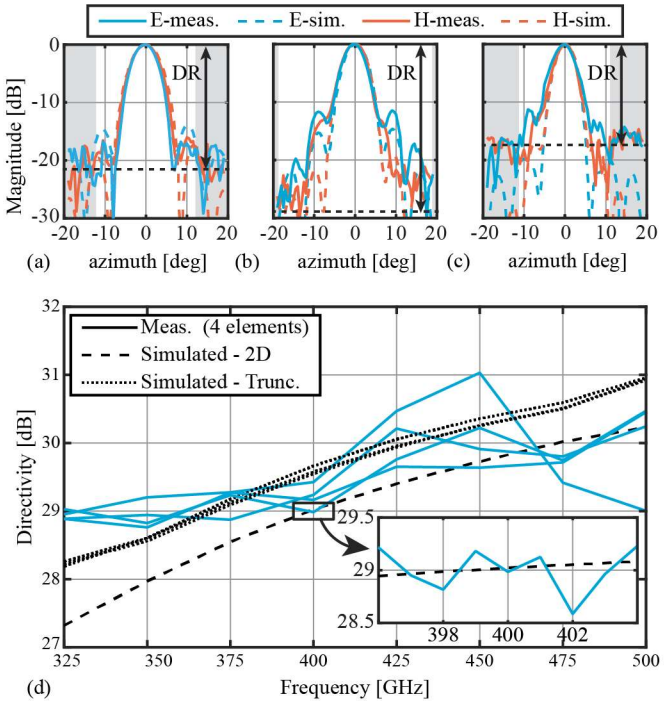

Fig. 4. Radiation patterns of one of the central pixels in the E- and H- planes at 325 GHz (a), 400 GHz (b) and 500 GHz (c) compared to simulations. The grey areas indicate the applied truncation for computing the directivity, the result of which is shown in (d) versus frequency for all four centrally located elements. The inset in (d) gives an indication of standing wave effects. For comparison, the simulated directivity was calculated using the full 2D pattern (dashed) and using the same truncation/cuts as the measurements (dotted).

to highlight the effects of standing waves present in the measurements [10]. Since this phenomenon is also spatially dependent, the variation of directivity between the elements can be (partially) explained by this effect.

D. System responsivity

To characterize the responsivity of the central array elements, their main beams were aligned to the horn antenna and the voltage response $\Delta V'$ was measured as a function of bias voltage and frequency. The responsivity was then extracted from this response using (1). A modulation frequency of 55 kHz was selected to avoid the effect the modulation frequency has on the voltage response at low bias voltages, and therefore maintain measurement precision, as was shown in Fig. 3(a).

Fig. 5(a) and (b) show the measured responsivity of the four central elements as a function of bias voltage and frequency, respectively. The dashed lines indicate the characteristics as expected from simulations, which were calculated using [5]:

$$\Re_{v,sys} = \eta_{ant}\eta_{\Omega}\Re_{v,det}. \quad (2)$$

The simulated system responsivity $\Re_{v,sys}$ contains the responsivity of the standalone detector $\Re_{v,det}$, the antenna efficiency η_{ant} (including the directivity) and the impedance match efficiency between the diodes and the antenna, η_{Ω}.

The mismatch between simulations and measurements shows the same trend as the directivity measurements and is below 1 dB (20.6%), except for the upper end of the examined frequency band. This indicates that the mismatch is mainly determined by the radiation characteristics of the array. The shaded area in Fig. 5(b) shows how a 5% variation in the diode series resistance and junction capacitance, which dominate the performance [5], affects the simulated responsivity. To first order, this variation only affects the detector responsivity and the impedance match efficiency, which can become more/less wideband. Note that any changes in the directivity following from a change in re-radiated power after reflection from the diodes [11] are not taken into account.

IV. Conclusions

In this contribution, we have presented a detailed approach on the implementation of an over-the-air characterization setup for measuring antenna-coupled direct-detectors at THz frequencies. Using an experimental analysis, it was shown how the modulation frequency can be selected to minimize the impact of the measurement procedure on the results, depending on the performance metrics of interest. The setup was used to measure the radiation patterns and responsivity of a CMOS-integrated connected array of direct-detectors in the WR2.2 band. Thanks to the methods described in this paper, the far-field of the array elements could be characterized down to a normalized magnitude of -30 dB at a distance of 20 cm. Furthermore, the measurement results are within 1 dB of simulations for the majority of the considered frequency band, both in terms of directivity and responsivity. This accuracy was maintained when considering multiple elements and when examining the effect of process variation.

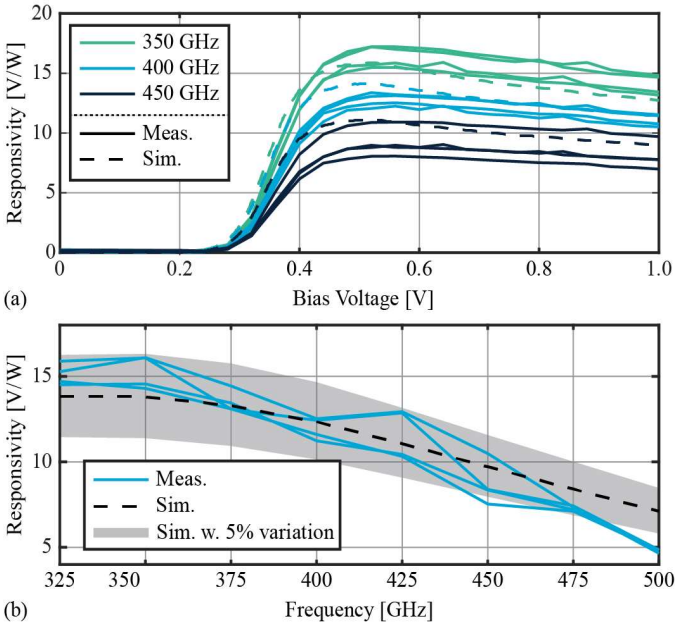

Fig. 5. Measured system responsivity of four central array elements as a function bias voltage (a), and versus frequency at a bias voltage of 1V (b), with the shaded range indicating the simulated responsivity following from a 5% variation in the diode parasitics.

References

[1] R. Al Hadi et al., "A 1 k-Pixel Video Camera for 0.7–1.1 Terahertz Imaging Applications in 65-nm CMOS," IEEE Journal of Solid-State Circuits, vol. 47, no. 12, pp. 2999-3012, Dec. 2012.

[2] S. L. van Berkel et al., "High Resolution Passive THz Imaging Array With Polarization Reusage in 22nm CMOS," 2019 44th International Conference on Infrared, Millimeter, and Terahertz Waves (IRMMW-THz), 2019, pp. 1-2, doi: 10.1109/IRMMW-THz.2019.8874183.

[3] M. Andree et al., "A Broadband Dual-Polarized Terahertz Direct Detector in a 0.13-µm SiGe HBT Technology," 2019 IEEE MTT-S International Microwave Symposium (IMS), 2019, pp. 500-503.

[4] K. Sengupta, D. Seo, L. Yang and A. Hajimiri, "Silicon Integrated 280 GHz Imaging Chipset With 4 x 4 SiGe Receiver Array and CMOS Source," in IEEE Transactions on Terahertz Science and Technology, vol. 5, no. 3, pp. 427-437, May 2015, doi: 10.1109/TTHZ.2015.2414826.

[5] S. v. Berkel et al., "Wideband Modeling of CMOS Schottky Barrier Diode Detectors for THz Radiometry," in IEEE Transactions on Terahertz Science and Technology, vol. 11, no. 5, pp. 495-507, Sept. 2021.

[6] M. Andree et al., "Broadband Modeling, Analysis, and Characterization of SiGe HBT Terahertz Direct Detectors," in IEEE Transactions on Microwave Theory and Techniques, vol. 70, no. 2, pp. 1314-1333, Feb. 2022.

[7] R. Han et al., "Active Terahertz Imaging Using Schottky Diodes in CMOS: Array and 860-GHz Pixel," in IEEE Journal of Solid-State Circuits, vol. 48, no. 10, pp. 2296-2308, Oct. 2013.

[8] M. Pelgrom, "Analog-to-Digital Conversion", 3rd ed., Springer, 2017, pp. 443.

[9] D. Cavallo and A. Neto, "A Connected Array of Slots Supporting Broadband Leaky Waves," in IEEE Transactions on Antennas and Propagation, vol. 61, no. 4, pp. 1986-1994, April 2013.

[10] M. Arias Campo et al., "On the Use of Fly's Eye Lenses with Leaky-Wave Feeds for Wideband Communications," in IEEE Transactions on Antennas and Propagation, vol. 68, no. 4, pp. 2480-2493, April 2020.

[11] N. Llombart et al., "Impact of Mutual Coupling in Leaky Wave Enhanced Imaging Arrays," in IEEE Transactions on Antennas and Propagation, vol. 56, no. 4, pp. 1201-1206, April 2008.